Optimal sensor placement using machine learning

R. Semaan[1]

Institute of fluid mechanics, Technical University of Braunschweig, Germany.[a)]

(Dated: 27 September 2016)

A new method for optimal sensor placement based on variable importance of machine learned models is proposed. With its simplicity, adaptivity, and low computational cost, the method offers many advantages over existing approaches. The new method is implemented on an airfoil equipped with a Coanda actuator. The analysis is based on flow field data obtained from 2D unsteady Reynolds averaged Navier-Stokes (URANS) simulations with different actuation conditions. The optimal sensor locations is compared against the current de-facto standard of maximum POD modal amplitude location, and against a brute force approach that scans all possible sensor combinations. The results show that both the flow conditions and the type of sensor have an effect on the optimal sensor placement, whereas the choice of the response function appears to have limited influence.

Keywords: Machine learning, optimal sensor placement, flow control

arXiv:1609.07885v1 [physics.flu-dyn] 26 Sep 2016

[a)]Electronic mail: r.semaan@tu-bs.de

I. INTRODUCTION

The number of sensors and their placement are critical for accurate model predictions and for closed-loop control applications. All known methods to determine the optimal sensor placement rely on either proper orthogonal decomposition (POD)[1–3], or on complicated optimization schemes[4,5]. The current study proposes a new general approach to determine the optimal sensor placement using variable importance of machine learned models. The new method circumvents the necessity for POD and for optimization, thereby reducing the complexity and the computational cost. The approach is applied on a circulation control wing under three different forcing conditions using two sensor types (pressure and shear).

Optimal sensor placement for structural health monitoring has been repeatedly studied (e.g. Xu et al.[4] , Padula & Kincaid[5], and Papadopulos & Garcia[6]). Most approaches start by simulating the structure using finite element methods (e.g. Guratzsch et al.[7]), or by modeling it (e.g. Fijani & Vatan[8], Lui & Tasker[9]). The optimal sensor placement is then usually determined with the aid of an optimization scheme (e.g. Xu et al.[4], Hamilton[10]). In principle, these methods are transferable to the fluid dynamics field, but due to their complexity (e.g. solving the algebraic Riccati equation) and numerical costs, they have only been implemented on simplified flows (e.g. Burns & Belinda[11], Allan et al.[12]). For engineering applications, only POD-based approaches have been employed.

The proper orthogonal decomposition has been widely used for a broad range of applications, such as image processing, signal analysis, data compression, and more recently optimal control. Essentially, POD is a linear procedure that seeks to find a deterministic vector field which has the maximum projection on a random vector field in a mean square sense. The deterministic functions constitute the orthogonal basis, which are determined as the solutions of an integral eigenvalue problem known as a Fredholm equation. These eigenfunctions are optimal in terms of representation of the energy present within the data.

A variety of POD-based methods have been used to infer optimal placement of sensors in fluid flows. Cohen et al.[1] used a heuristic approach to determine the sensor locations by placing them at the extrema of the POD modes, whereas Willcox[2] and Yildirim et al.[3] used Gappy POD. Gappy POD, developed by Everson & Sirovich[13], can reconstruct incomplete datasets by solving an additional linear system. The Gappy POD results were similar to the heuristic approach, and the optimum sensor locations almost coincided with the modes

extrema. A similar approach was also used by Mokhasi and Rempfer[14]. Kumar et al.[15] used linear stochastic estimation (LSE) to infer the sensor positions by minimizing the error between the LSE predictions and the reference POD mode amplitudes. Their approach contained large uncertainties caused by the limited sensitivity of the LSE predictions towards sensor positions. As previously mentioned, all existing approaches for engineering applications rely on POD for their sensor placement. However, proper orthogonal decomposition is sometimes difficult (e.g. very large mesh from LES) or impossible (no spatial field data, or steady flow) to compute. Moreover, using a finite number of POD mode amplitudes as state estimators is sometimes inaccurate, as the relevant aerodynamic properties are not always linearly related to the small subset of selected modes. This issue is compounded by the fact that all POD-based methods require a minimum number of sensors, which must be always equal or larger than the total number of considered modes. This means, for a flow with a shallow modal energetic distribution, one is compelled to use a large number of sensors.

Beside the methodological constraints, all the aforementioned studies failed to investigate the effect the sensor type (e.g. pressure sensor, or shear stress sensor) has on the placement. In addition, the optimal sensor distribution was only determined for a single flow condition, and thus does not capture the likely variations in the optimal sensor positions with varying flow/actuation conditions.

This study introduces a new machine learning based approach to identify optimal sensor positions for a range of conditions and using two different type of sensors. The method is implemented on three URANS numerical simulations of a circulation control wing under different forcing conditions. The circulation control wing is shown in figure 7, where the highly deflected Coanda flap and the blowing slit can be seen. This work is part of a larger project that aims to improve the actuation efficiency of airfoils with blown flaps by means of closed-loop control. Beside the numerical and theoretical investigations, the research project entails a water tunnel experiment, which can integrate an array of pressure and hot film sensors.

II. OVERVIEW OF METHOD

Machine learning encompasses many data-driven algorithms and methods. A supervised learning algorithm takes a set of input data and corresponding outputs (responses), and

trains a model to generate predictions for the response to new input data. For this study, two supervised machine learning regression algorithms were evaluated: support vector machine[16] (not shown), and random forests[17]. It is important to note that the proposed method can be implemented using any algorithm. Ultimately, random forests was selected due to its lower out-of-bag (OOB) error and its inherent OOB randomization, which is convenient for variable importance (see § II E). The out-of-bag error is the prediction error of machine learning models that utilize bootstrap aggregation. Specifically, it is the mean prediction error of the data left out from the bagging procedure. This section describes the overall approach used to predict the flow and to determine the optimal sensor positions. All algorithms and data processing are implemented using Statistics and Machine Learning Toolbox™ from Matlab.

A. Random forests

The random forests algorithm belongs to the family of Classification and Regression Trees (CART), where a decision tree with binary splits that maximize the information gained is constructed. Details on the algorithm can be found in many publications on the subject (e.g. Breiman[17], Hastie et al.[18]). Only an overview is provided here.

Random forests is an ensemble method that builds multiple regression trees by repeatedly resampling training data with replacement, and averaging the results. Each tree model predicts the response variable by learning simple if-then-else decision rules from the data. The random sampling has two main benefits. First, it increases tree diversity, and thus improves robustness of the prediction. Second, it is less prone to overfitting, since at each split only a subset of the features is used. Since there is no limitation on the tree depths in random forests, the algorithm requires only one parameter to set: the number of decision trees, N_{RF}. The necessary number of decision trees can be evaluated by tracking the out-of-bag error, which is directly obtained from the bootstrapping procedure. In random forests, there is no need for cross-validation. Each tree is constructed using a different bootstrap sample with one-third of the samples left out from each tree. Figure 1 shows the regression error rate as function of the number of trees for one of the models in this paper. As the forest grows larger, the accuracy increases but with diminishing returns. The error rate decreases drastically between 1 and 30, followed by some fluctuations and small gradual improvement as N_{RF} increases. As the difference in training times between the various sized

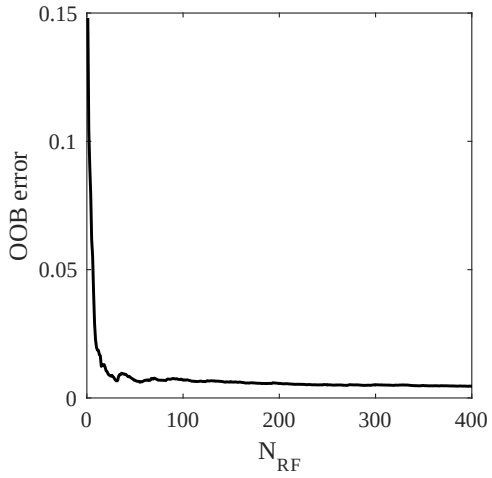

FIG. 1: Out-of-bag error versus the number of trees, N_{RF}.

trees is negligible, N_{RF} is set to 200 for good accuracy.

B. Data sampling and acquisition

The first step in machining learning is to generate a suitable training dataset. Here we have used numerical simulations due to the ease of extracting data everywhere in the field and especially over the model surface. Since this study's ultimate objective is to perform closed-loop control, it is necessary to investigate the flow and to determine the optimal sensor locations under different flow conditions. Details of the numerical simulations and the different test cases are presented in section III.

C. Input formulation

The input training data for the current machine learned models are the instantaneous signals of 96 surface sensors. In order to obtain practical results in an engineering sense, sensor locations are restricted to the model surface, i.e. no sensors are allowed in the flow. The region over the Coanda flap, shown in figure 2, is the most sensitive to changes occurring in the wake and to changes originating from the Coanda jet. The range of possible sensor locations is therefore further restricted to the flap upper surface and to a small region over the jet exit slot. All the 96 considered possible sensor locations are shown by the gray marks in figure 2. Two types of input from these sensors is considered: pressure p, and wall shear

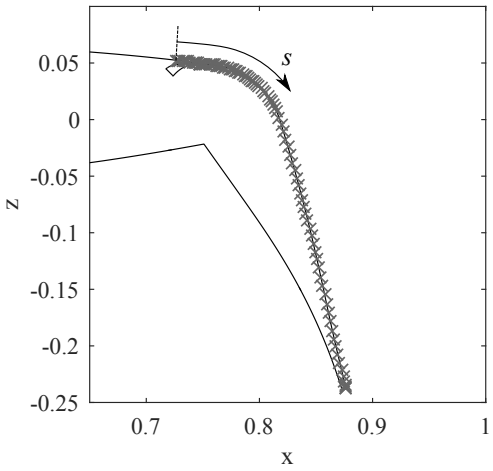

FIG. 2: All possible sensor locations over the highly deflected flap. Also shown is the curvilinear coordinate s along the flap surface with its origin at the first possible sensor location.

stress coefficient C_f. Also shown is the curvilinear coordinate s along the flap surface with its origin at the first possible sensor location.

D. Response function selection

The state of a flow can be characterized through a multitude of metrics, which constitute the response functions for this machine learning problem. The choice of the metric depends on the problem's objectives and on the data availability. For the current flow, several response functions that characterize the state of the flow are conceivable. In the following, three response functions are presented.

1. Proper orthogonal decomposition

Proper orthogonal decomposition (POD) methods are powerful tools for data analysis aimed at obtaining low-dimensional approximate descriptions of a high-dimensional problem. POD is the most optimal modal decomposition in the sense that no other decomposition of the same order captures an equivalent amount of kinetic energy. POD of a 2D flow assumes

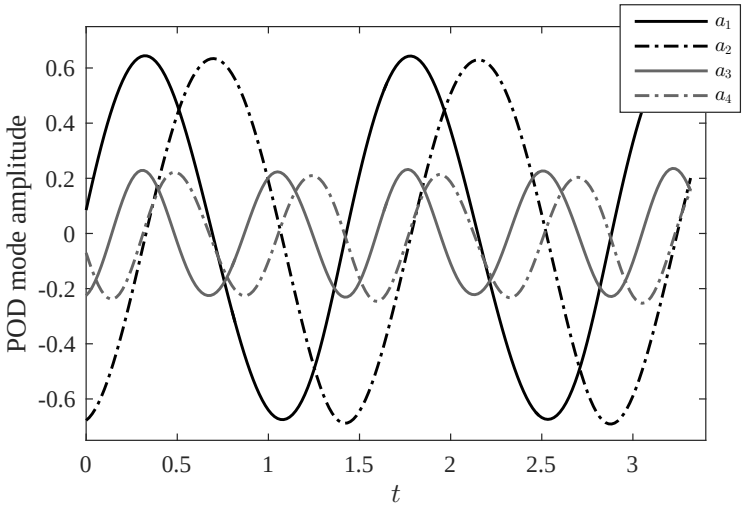

FIG. 3: The first four POD mode amplitudes for the unactuated case.

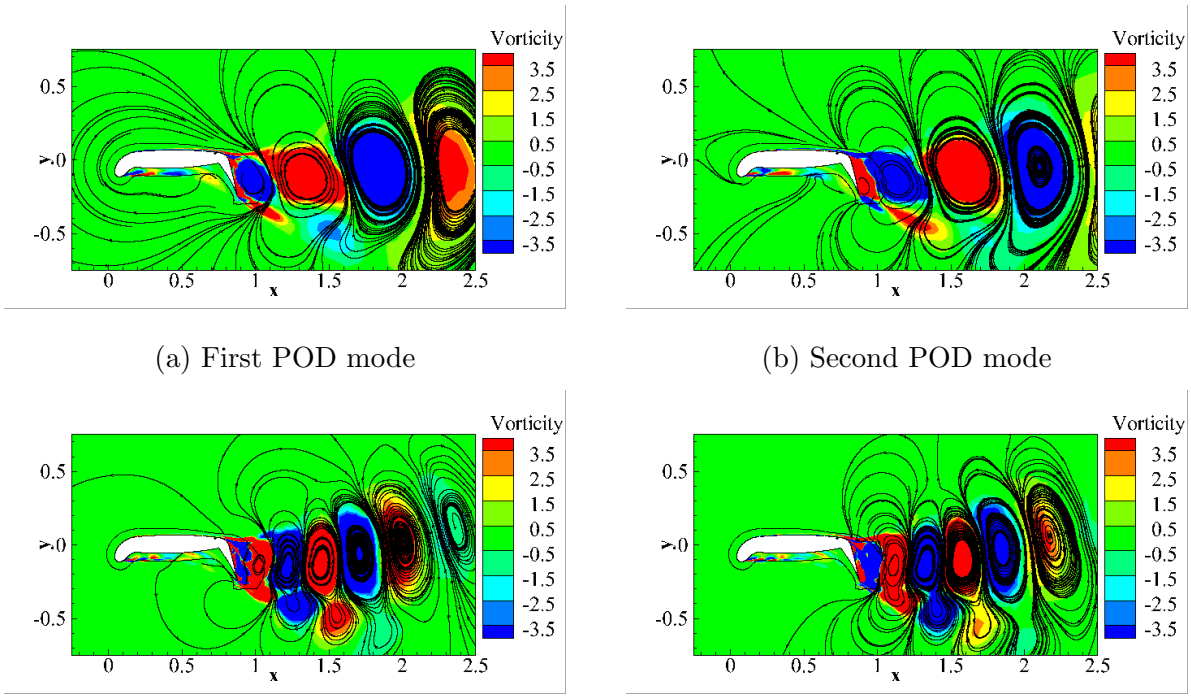

(a) First POD mode

(b) Second POD mode

(c) Third POD mode

(d) Fourth POD mode

FIG. 4: The first four POD modes visualized by the vorticity fields and vortex lines.

that the velocity fluctuations $\tilde{u}$ can be decomposed as

$$\tilde{u}(x,y,t) = \sum_{k=1}^{N} a_k(t)\,\phi_k(x,y)\,, \tag{1}$$

where ϕ_k are the POD modes, a_k are their corresponding amplitudes, and N is the total number of modes. The method of snapshots as introduced by Sirovich[19] is used to perform the decomposition. Here, the mode amplitudes are first determined from the solution of the eingenvalue problem

$$C\,A = \lambda A\,, \tag{2}$$

where λ is the eigenvalues diagonal matrix, and A is the eigenvector matrix containing the mode amplitudes. The cross-correlation matrix C is defined as

$$C_{ij} = \frac{1}{N}\langle \tilde{u}(x,y,t_i)\cdot\tilde{u}(x,y,t_j)\rangle\,, \tag{3}$$

with $\langle\cdot\rangle$ the spatial averaging operator. The POD modes are then determined by projecting the mode amplitudes onto the snapshots and normalizing

$$\phi_k(x,y) = \frac{1}{N\lambda_k}\sum_{i=1}^{N} a_k^i\, u(x,y,t_k)\,. \tag{4}$$

The POD mode amplitudes represent the temporal evolution of the modes and by extension of the flow. The POD mode amplitudes, or linear combinations thereof, are therefore chosen as response functions. In this study, only the first four modes are considered, which capture more than 90% of the total kinetic energy for all three test cases. Their mode amplitudes are shown in figure 3 for the unactuated case, where mode pairing (mode 1–2, and mode 3–4) typical for highly shedding flows can be observed. The corresponding first four modes for this unactuated case are presented in figure 4, visualized by their vorticity fields and vortex lines. The first two POD modes represent von Kármán vortex shedding. The third and fourth modes resolve the first harmonic of the dominant shedding frequency. Proper orthogonal decomposition was performed using the xAMC software package.

2. Lift coefficient

The lift coefficient is usually the most relevant parameter in aircraft aerodynamics. It is therefore the ideal metric for a response function. The lift coefficient can be experimentally acquired from a balance or from the surface pressure distribution. Numerically, it is directly obtained from the solution.

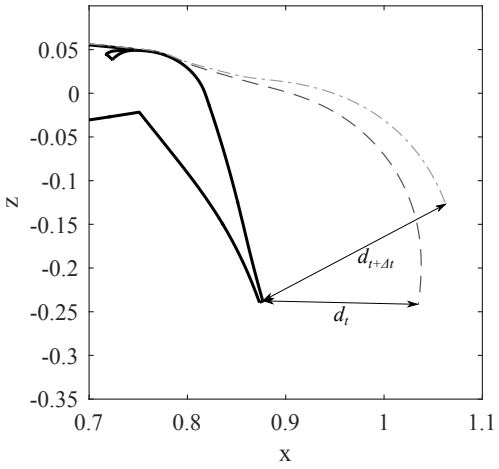

FIG. 5: Schematic illustrating streamline tracking.

3. Streamline tracking

The third tested metric that reflects the state of the flow is the streamline distance d. The process is illustrated in figure 5. Similar to experimentally tracking the tip of a long weightless tuft, the tip of a constant-length streamline is tracked in real time by computing the distance d between the airfoil trailing edge and the streamline tip. The streamline length was chosen such that the distance d is zero for an attached state. The change in the distance reflects the state of the wake, where, for example, large values and high fluctuations indicate a separated flow.

E. Optimal sensor placement

The optimal sensor positions are simply determined as the most important variables of the machine learned model. Since each sensor signal is treated as an input variable, the most important variables are consequently the optimal sensors. In data mining applications the input variables are rarely equally relevant. Often only few of them affect the response; and the rest can be excluded. Several methods can be used to rank the variable importance, such as the Gini splitting index and the OOB randomization. In this study, the OOB randomization method was selected for its ease of implementation as a byproduct of random forests, and for its well documented accuracy for variables of the same type[20]. The OOB

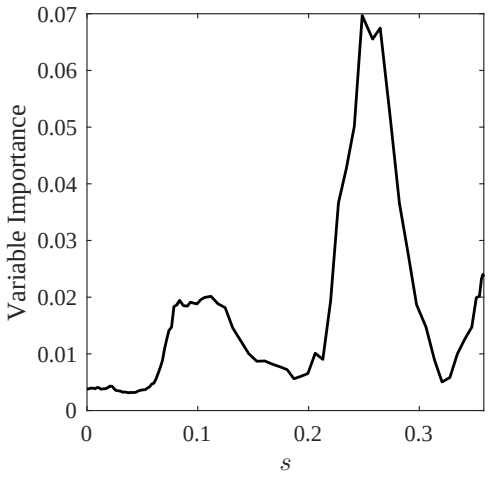

FIG. 6: Variable (sensor) importance distribution over the flap to predict a_1 for the unactuated case.

randomization returns an array containing a measure of importance for each predictor variable. This measure is computed as the increase in prediction error for any variable as their values are permuted across the out-of-bag observations. This process is repeated for every tree, then averaged over the entire ensemble and divided by the standard deviation over the entire ensemble.

An example of the variable (sensor) importance distribution over the flap is presented in figure 6 to predict a_1 for the unactuated case. The distribution shows three regions of high relevance: $s \approx 0.25$, $s \approx 0.35$ (flap tip), and $s \approx 0.1$ in order of their importance.

III. NUMERICAL SETUP

The present investigations are based on three two-dimensional URANS numerical simulations of an airfoil equipped with a Coanda flap. The test cases are selected for their different aerodynamic characteristics, which range from fully separated to nearly fully attached. In the following, the airfoil configuration is introduced (§ III A), the numerical setup is detailed (§ III B), and the test cases and their characteristics are presented (§ III C).

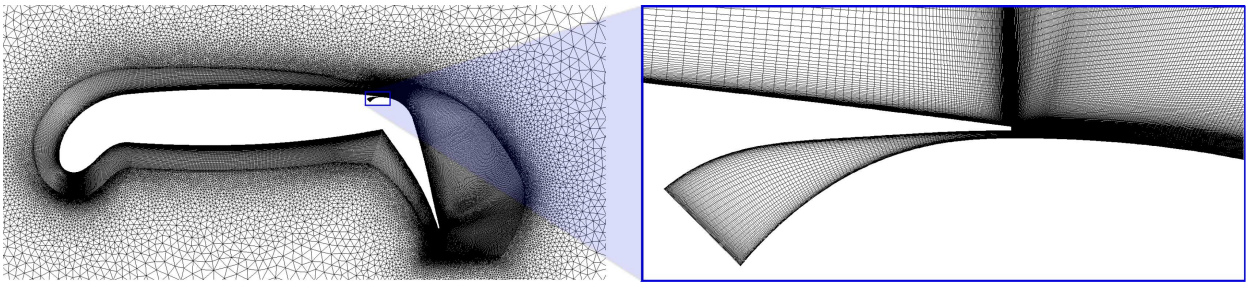

FIG. 7: Part of the numerical mesh surrounding the modified DLR F15 airfoil with a close-up of the actuation duct.

A. Configuration

The high-lift configuration, shown in figure 7, is a modified DLR F15 airfoil equipped with a highly deflected Coanda flap and a droop nose. The details of the airfoil design are described in Burnazzi & Radespiel[21] and Jensch et al.[22], where the objective was to accomplish high lift coefficients during take-off and landing. The leading edge geometry was reached after an iterative process that improved the airfoil stall behavior, which is ruled by the suction peak. The highly deflected flap at 65° has a chord length of $c_{\mathrm{fl}} = 0.25\,c$, where c is the main airfoil chord length with the retracted flap. The numerical simulations are performed at Mach number Ma = 0.15, and Reynolds number $\mathrm{Re} = U_\infty c/\nu = 12 \cdot 10^6$, where ν is the kinematic viscosity of the fluid. These flow parameters correspond to the expected conditions during landing.

As this study is part of a larger project aimed at increasing the actuation efficiency of a circulation control wing, an unsteady periodic component is superimposed onto the steady Coanda blowing component (Oyler and Palmer 1972, Jones et al. 2002). Numerically, the periodic Coanda blowing is performed by pulsating the pressure boundary condition at the base of the actuation chamber (see close-up in figure 7).

B. Unsteady Reynolds averaged Navier-Stokes simulations

The computational fluid dynamics (CFD) solver employed to perform the analysis is the DLR TAU-Code[23,24]. The two-dimensional Unsteady Reynolds Averaged Navier-Stokes (URANS) equations are solved using a finite volume approach. The discretization schemes are the central scheme and the second order upwind Roe scheme for the mean-flow invis-

TABLE I: Summary of the actuation conditions for the three test cases.

F^+	$C_{\mu 0}$	$C_{\mu 1}$	Reference name
0	0	0	Unactuated
1	0.011	0.0015	Weakly actuated
1	0.035	0.0144	Moderately actuated

cid flux and the convective flux of the turbulence transport equation, respectively. The turbulence model is that of Spalart–Allmaras with curvature correction[25], which allows the one-equation turbulence model to maintain a good accuracy in regions where the streamlines have high curvature. This characteristic is fundamental for the simulation of the Coanda phenomenon, which is based on the equilibrium between the inertial forces and the momentum transport in the direction normal to the convex surface[26]. The numerical scheme and the turbulence model were previously assessed by comparing the results to wind tunnel experiments[27,28]. The lift, drag, and pitching moment coefficients are determined by integrating the pressure and shear stress distributions over the airfoil surface. The contribution from the added jet momentum is not included.

The mesh is composed of a structured and an unstructured region, as the close-up in figure 7 shows. The outer unstructured mesh has a C-block topology and extends 50 chord lengths in all directions. The structured grid extends from the airfoil surface outward to cover the region where the main viscous phenomena occur. The viscous sub-layer is also resolved with $y_+ < 1$ everywhere over the airfoil surface. An important characteristic of the grid is the high density along the pressure side, where the stagnation point can be located, far from the leading edge. The structured region also extends over a large area behind the highly-deflected flap, in order to accurately capture the wake dynamics. Both, the trailing edge and the edge of the blowing slit, are discretized by means of a local C-block topology.

C. Test cases

In order to test the proposed method under different flow conditions, three test cases characterizing different flow separation states are numerically simulated. These test cases, summarized in table I, are characterized by three parameters, $C_{\mu 0}$, $C_{\mu 1}$ and F^+, of which

only variations in $C_{\mu 0}$ and $C_{\mu 1}$ are considered. The non-dimensional actuation frequency F^+, defined as[29,30]

$$F^+ = \frac{f^a \, c_{\mathrm{fl}}}{U_\infty}, \tag{5}$$

where f^a is the actuation frequency, U_∞ is the free stream velocity, and c_{fl} is the flap chord length, is kept constant. For both the weak and moderate blowing cases, it is set at $F^+ = 1$ (i.e. $f^a = 204$ Hz), as recommended by Nishri and Wygnanski[31] based on parametric studies. The periodic blowing intensity can be prescribed as

$$c_\mu(t) = \frac{U_{\mathrm{J}}(t) \, \dot{m}_{\mathrm{J}}(t)}{\frac{1}{2} \, \rho \, U_\infty^2 \, S_{\mathrm{ref}}}, \tag{6}$$

where $\dot{m}_{\mathrm{J}}$ is the jet mass flow rate, U_{J} is the jet averaged velocity across the slit, and S_{ref} is the reference area. The subscript ∞ denotes far field conditions. For the current periodic actuation, the momentum coefficient can be expressed as $c_\mu(t) = C_{\mu 0} + C_{\mu 1} \cos(2 \, \pi \, f^a \, t)$, where $C_{\mu 0}$ is the steady mean and $C_{\mu 1}$ is the oscillation amplitude. This yields a range of mean momentum coefficients between $C_{\mu 0} = 0$ and 0.035. The oscillation amplitudes for the weakly and for the moderately actuated cases are $C_{\mu 1} = 0.0015$ and 0.0144, respectively. The angle of attack is kept constant at 0° for all cases.

IV. RESULTS AND DISCUSSION

The previous sections discussed the method and the numerical setup. In this section, the results for the circulation control wing are presented. The powerful predictions of the machine learned models are first shown. Optimal sensor positions are then presented for the different test cases, for the different state estimators and for two types of sensors.

A. Unsteady flow estimation

Albeit uncommon, machine learning has been previously employed in the field of fluid dynamics. It has been successfully implemented in closed-loop flow control (e.g. Bernhardt & Williams[32], and Faller et al.[33]), and in turbulence modeling applications (e.g. Ling & Templeton[34], and Tracey et al.[35]). To the author's knowledge, machine learning has not been used to infer optimal sensor placement.

Before presenting the optimal sensor placement results, it is relevant to assess the prediction accuracy of the machine learned models upon which the method is based. Figure

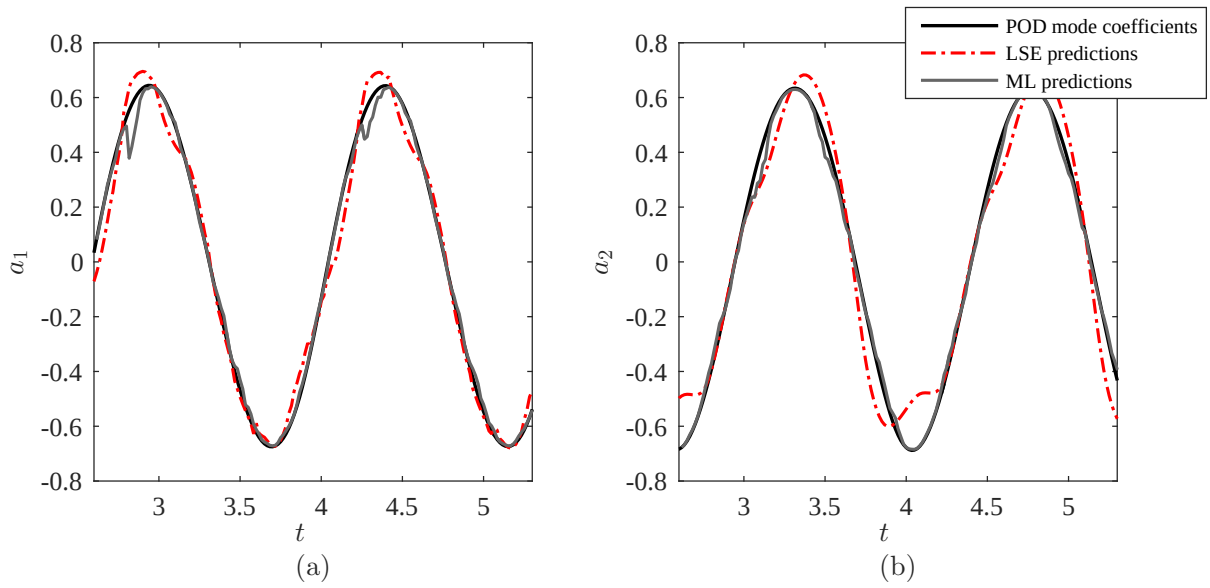

FIG. 8: Reference POD (black), linear stochastic (red) and machine-learning (gray) estimated mode coefficients using two optimal pressure sensors to estimate a_1 and a_2 for the unactuated case.

8 presents the first two reference POD (black) and the predicted machine-learned (gray) mode coefficients using two optimal pressure sensors for the unactuated case. Also shown are the linear stochastic estimation (LSE) predictions[15] (red) using also two optimal pressure sensors. The accuracy of the machine learned model is clear; the predictions follow the reference POD mode coefficients closely. Compared to the LSE results, the present models deliver ~68% and ~93% smaller mean square error for a_1 and a_2, respectively. The small deviations and the overall prediction accuracy can be further improved by invoking additional techniques, such as sliding window methods or hidden Markov models[36]. Such techniques are not utilized in the current study, as the focus is on optimal sensor placement.

Further validation of the models is presented in figure 9 for two different state estimators. The figure shows the reference (black) and estimated (gray) (a) lift coefficient C_l and (b) streamline distance d using two optimal pressure sensors for the moderately actuated case. The results are also in a very good agreement with the reference data. The predictions are indiscernible from the URANS results. Good agreement was also documented for other test cases and response functions.

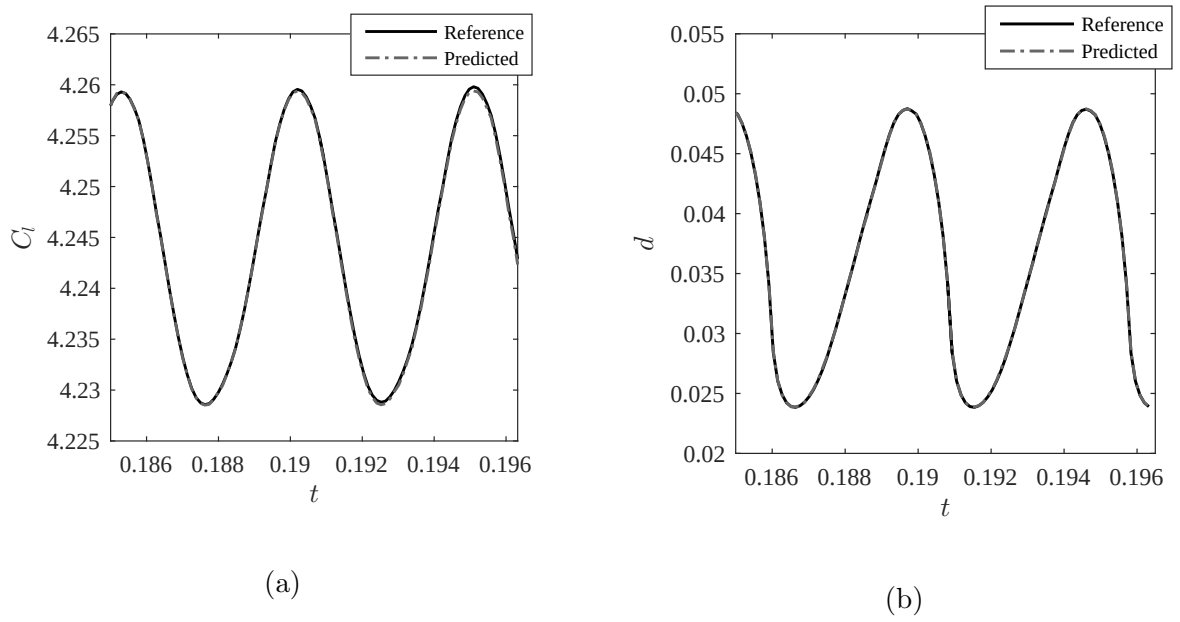

(a) (b)

FIG. 9: Reference (black) and estimated (gray) (a) lift coefficient C_l and (b) streamline distance d using two pressure sensors for the moderately actuated cases.

B. Optimal sensor placement

1. Method validation

Whether heuristic[1] or mathematical[2,3], POD-based approaches for optimal sensor placement positions the sensors at the extrema of the POD modes. Since we have restricted the possible sensor positions to the aft surface of the airfoil, this method yields optimal locations at the maximum modal surface values. The results using this approach (✯) are presented in figure 10 alongside those using the proposed variable importance method (◁) for a single pressure sensor. Also shown, are the optimal sensor positions using brute force permutations over all sensors (□). The brute force approach generates a machine learned model for each possible sensor (or for each possible sensor combination for multiple sensors configuration) and computes its OOB error. The optimal sensor location is then determined as the position with the lowest OOB error. As the figure shows, the sensor positions using the variable importance method are always similar to those from the brute force approach. This is not surprising since the bootstrapping in random forest is similar to the permutations in the brute force method. Except for a_4, all three methods yield comparable sensor

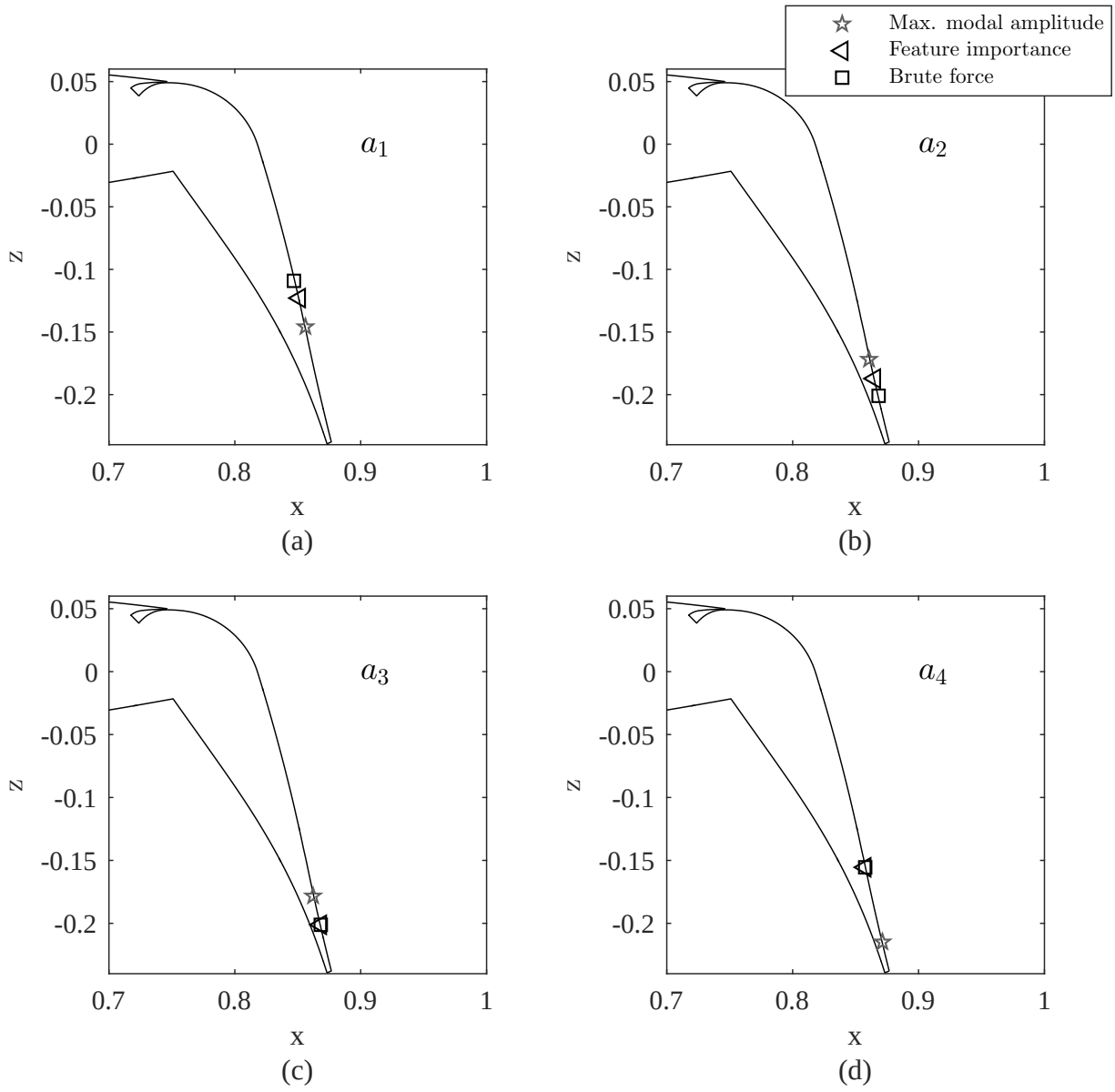

FIG. 10: Optimal pressure sensor position to predict the first four POD mode coefficients for the unactuated case using the maximum modal surface value (✯), the sensor with the highest feature importance (◁), and the brute force permutation (□).

positions, thus providing confidence in the proposed method.

2. Effect of response function choice and of flow conditions on optimal sensor placement

As introduced in section II D, the state of the flow can be inferred using various metrics. The effect of three different response functions on the optimal pressure sensor positions for the three test cases is illustrated in figure 11. The symbol $\sum a_i$ designates the sum of the first 4 POD mode coefficients, whereas C_l and d denote the lift coefficient and the streamline distance, respectively. As the figure shows, the sensor positions using $\sum a_i$ and d are surprisingly analogous for all three cases. This suggests that the streamline distance delivers similar information about the instantaneous flow state as the POD mode coefficients. The sensor locations using C_l differ slightly than those from the other two response functions, especially for the moderately actuated case. This difference is not entirely unexpected as the relation between C_l and the other two response functions is not necessarily linear. In fact, C_l has been shown to be highly nonlinearly related to the mode coefficients for this flow[37].

The effect flow conditions have on the optimal sensor position can be also observed in figure 11. As the flow gradually changes from fully separated to almost fully-attached, the optimal sensor position also changes. For all cases, the sensor placement appears to favors locations closer to the trailing edge than to the flap shoulder. A clear trend in the position evolution is however difficult to discern. Such change in optimal sensor positions is clearly problematic for closed-loop flow control experiments, which experience a range of conditions. A compromise that best captures the flow state under the various conditions is therefore necessary. This compromise is obtained by combining the data from the three test cases (using the same record length for each case) into a single dataset and repeating the same procedure as before. Alternatively, one can perform one long simulation with varying forcing conditions (such as with chirp forcing). Figure 12 presents the optimal pressure sensor position for the three response functions for the combined test case. The sensor positions using $\sum a_i$ and d are again similar. They are located near the tip, which is similar to the weakly actuated case. The sensor location using C_l again differs from the results of the two other response functions. It is located at approximately the same location as for the unactuated case.

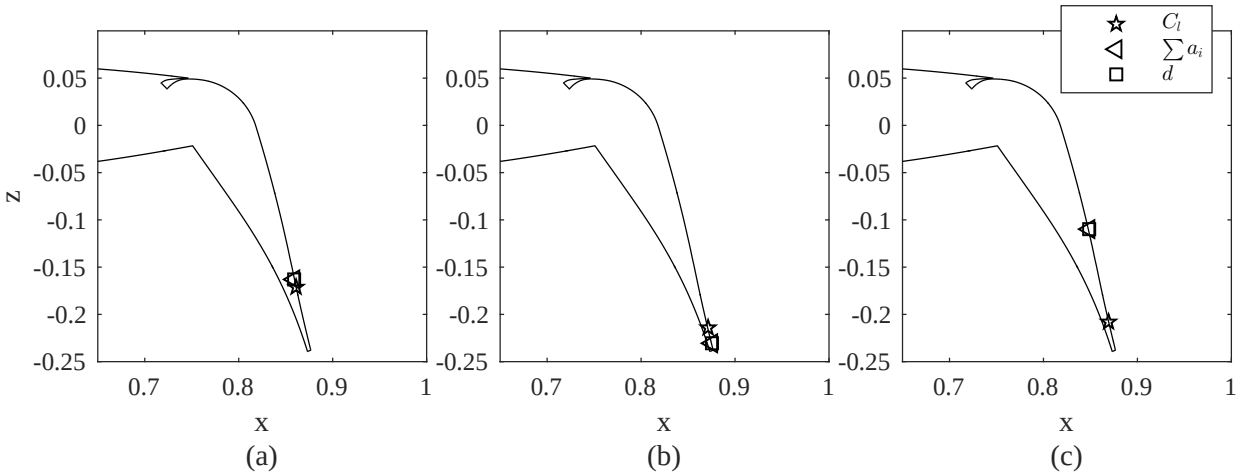

FIG. 11: Optimal pressure sensor position for the three response functions for the (a) unactuated, (b) the weakly actuated and (c) the moderately actuated test cases.

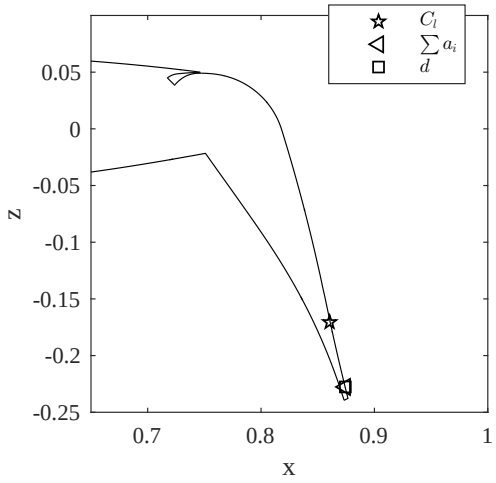

FIG. 12: Optimal pressure sensor position for the three response functions for the combined test case.

3. Effect of sensor type on optimal sensor placement

The sensor type plays an important role in an experiment, whether to understand the flow behavior or to use as input for closed-loop control. Typical sensors for aerodynamic applications measure either pressure or shear stress. In order to simulate the signal of an experimental hot-film sensor which is insensitive to the flow direction, the absolute value of the numerical wall shear stress data was initially used. This step, however, was superfluous

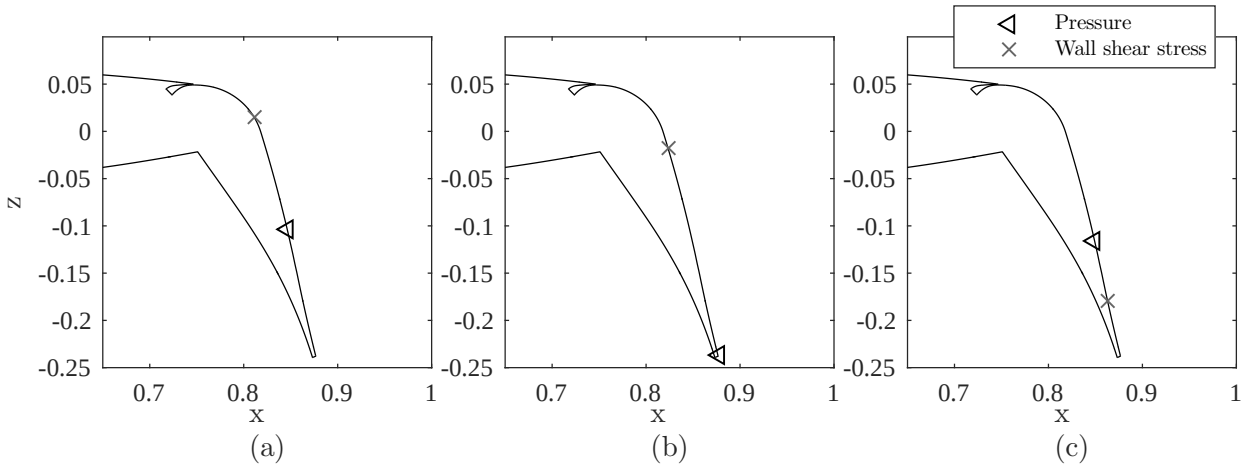

FIG. 13: Optimal sensor position to estimate a_2 using two sensor types for the (a) unactuated, (b) the weakly actuated, (c) and the moderately actuated test cases.

as the results between the sensor locations using the raw and the absolute values are similar. Figure 13 presents the optimal sensor positions to estimate a_2 using either a pressure or a wall shear stress sensor for the (a) unactuated, (b) the weakly actuated, (c) and the moderately actuated test cases. As the figure shows, the optimal sensor position clearly depends on the sensor type. For all three test cases, the pressure sensor location shifts between the middle and tip of the flap. On the other hand, the optimal shear stress sensor is located around the flap shoulder for the unactuated case and gradually shifts towards the tip with higher actuation intensity. This difference between the two sensor types can be attributed to the different flow phenomena they respectively capture; the wall shear stress sensor appears to be best positioned at the start of the separation region, whereas the optimal pressure sensor is located at the maximal modal value over the flap surface. The optimal wall shear stress sensor location does not seem to be correlated with the POD extrema. This obviously has important consequences on the design of POD model-based closed-loop control experiments using hot-films.

V. CONCLUSIONS

In this study a new machine learning-based method for optimal sensor placement is introduced. The method first constructs machine learned models from a range of input

sensors to predict a response function. The optimal sensor positions are then determined as the most relevant features through variable importance ranking. The method offers several advantages over existing alternatives: it is simple, adaptable, and computationally inexpensive. The chosen machine learning algorithm is random forest, due to its accuracy and inherent randomization.

The proposed approach is implemented on a circulation control wing for a range of actuations conditions. The analysis is based on three two-dimensional unsteady Reynolds averaged Navier-Stokes (URANS) simulations of the airfoil, which is equipped with a drooped nose and with a Coanda flap. The three simulations are conducted at different actuation frequencies and blowing intensities, yielding different flow conditions.

The model prediction accuracy is validated through the low out-of-bag error and by comparing the model output to reference data. Good agreement between the model predictions and the reference results is observed for three response functions: the POD mode amplitudes, the lift coefficient, and the streamline distance. Using the OOB randomization of random forests, the variable importance and hence the optimal sensor positions are determined. The results are compared against the extrema modal amplitude and against a brute force permutations approach for the first four POD mode amplitudes. The three methods yield comparable sensor positions, providing confidence in the proposed approach.

The effect of the response function choice on the sensor placement is examined. The results suggest that as long as the response function is physical and reflect the state of the flow, its type has little influence on the optimal sensor positions. On the other hand, flow conditions clearly affect the sensor placement. For a flow with varying conditions, we recommend training data that simulate the entire range of expected conditions. The optimal sensor position would then be a compromise for the entire range. The type of sensor has also an effect on the sensor positioning. Recommendations concerning the type of sensor are strongly related to the experiment's objectives. If the objective is solely the physical understanding of the flow, then either pressure or hot-film sensors can be used. If the objective is closed-loop flow control, then a pressure sensor might be better suited since its sensitivity to varying flow conditions appears to be lower. The recommendation for pressure sensor stems also from a practical perspective, as hot-film sensors are usually difficult to calibrate.

To the best of our knowledge, the present study is the first to introduce a machine-learning

based approach for optimal sensor placement. The proposed method can be employed in any fluid dynamics application and even in other fields such as structural health monitoring. It can be exploited to design better experiments and control laws.

REFERENCES

[1]K. Cohen, S. Siegel, D. Wetlesen, J. Cameron, and A. Sick, Effective sensor placements for the estimation of proper orthogonal decomposition mode coefficients in von Kármán vortex street, Journal of Vibration and Control **10**, 1857 (2004).

[2]K. Willcox, Unsteady flow sensing and estimation via the gappy proper orthogonal decomposition, Computers & Fluids **35**, 208 (2006).

[3]B. Yildirim, C. Chryssostomidis, and G. E. Karniadakis, Efficient sensor placement for ocean measurements using low-dimensional concepts, Ocean Modelling **27**, 160 (2009).

[4]K. Xu, P. Warnitchai, and T. Igusa, Optimal placement and gains of sensors and actuators for feedback control, Journal of Guidance, Control, and Dynamics **17**, 929 (1994).

[5]S. L. Padula and R. K. Kincaid, Optimization strategies for sensor and actuator placement, Technical report, NASA, TM-1999-209126, 1999.

[6]M. Papadopoulos and E. Garcia, Sensor placement methodologies for dynamic testing, AIAA Journal **36**, 256 (1998).

[7]R. F. Guratzsch, S. Mahadevan, C. L. Pettit, and M. M. Derriso, Sensor placement optimization for SHM systems under uncertainty, in *AIAA Paper 2005–2217*, 2005.

[8]A. Fijany and F. Vatan, A new method for sensor placement optimization, in *AIAA Paper 2005–3715*, 2005.

[9]C. Liu and F. A. Tasker, Sensor placement for multi-input multi-output dynamic identification, in *AIAA Paper 95–1114–CP*, 1995.

[10]H. Hamilton, Optimal sensor/actuator placement using an adjoint method, in *AIAA Paper 2007–1420*, 2007.

[11]J. A. Burns and B. B. King, Optimal sensor location for robust control of distributed parameter systems, in *IEEE Conference on Decision and Control*, volume 4, pp. 3967–3967, 1994.

[12]B. Allan, J. Juang, A. Seifert, L. Pack, and D. Brown, Closed-loop separation control using oscillatory flow, Technical report, ICASE report, 2000.

[13]R. Everson and L. Sirovich, Karhunen–Loeve procedure for gappy data, Journal of the Optical Society of America **12**, 1657 (1995).

[14]P. Mokhasi and D. Rempfer, Optimized sensor placement for urban flow measurement, Physics of Fluids **16**, 1758 (2004).

[15]P. Kumar, Y. M. El Sayed, and R. Semaan, Optimized sensor placement using stochastic estimation for a flow over a 2D airfoil with coanda blowing, in *AIAA Paper 2014–2101*, 2014.

[16]C. Cortes and V. Vapnik, Support-vector networks, Machine Learning **20**, 273 (1995).

[17]L. Breiman, Random forests, Machine Learning **45**, 5 (2001).

[18]T. Hastie, R. Tibshirani, and J. Friedman, The elements of statistical learning, second edition, NY Springer (2013).

[19]L. Sirovich, Turbulence and the dynamics of coherent structures, Quarterly of Applied Mathematics **XLV**, 561 (1987).

[20]C. Strobl, A.-L. Boulesteix, A. Zeileis, and T. Hothorn, Bias in random forest variable importance measures: Illustrations, sources and a solution, BMC Bioinformatics **8**, 1 (2007).

[21]M. Burnazzi and R. Radespiel, Design and analysis of a droop nose for coanda flap applications, AIAA Journal of Aircraft **51**, 1567 (2014).

[22]C. Jensch, K. C. Pfingsten, R. Radespiel, M. Schuermann, M. Haupt, and S. Bauss, Design aspects of a gapless high-lift system with active blowing, in *58. Deutscher Luft- und Raumfahrtkongress, Aachen, Germany*, 2009.

[23]N. Kroll, C. C. Rossow, D. Schwamborn, K. Becker, and G. Heller, MEGAFLOW-a numerical flow simulation tool for transport aircraft design, in *ICAS Congress*, pp. 1–105, 2002.

[24]D. Schwamborn, T. Gerhold, and R. Heinrich, The DLR TAU-code: Recent applications in research and industry, in *European Conference on Computational Fluid Dynamics, ECCOMAS CFD*, 2006.

[25]M. L. Shur, M. K. Strelets, A. K. Travin, and P. R. Spalart, Turbulence modeling in rotating and curved channels: Assessing the Spalart-Shur correction, AIAA Journal **38**, 784 (2000).

[26]K. C. Pfingsten, C. Jensch, K. V. Körber, and R. Radespiel, Numerical simulation of the flow around circulation control airfoils, in *First CEAS European Air and Space Conference,*

Berlin, 2007.

[27]K. C. Pfingsten, R. D. Cecora, and R. Radespiel, An experimental investigation of a gapless high-lift system using circulation control, in *Katenet II Conference, Bremen*, 2009.

[28]K. C. Pfingsten and R. Radespiel, Experimental and numerical investigation of a circulation control airfoil, in *AIAA Paper 2009–533*, 2009.

[29]A. Seifert, A. Darabi, and I. J. Wyganski, Delay of airfoil stall by periodic excitation, Journal of Aircraft **33**, 691 (1996).

[30]A. Seifert, D. Greenblatt, and I. J. Wygnanski, Active separation control: an overview of Reynolds and Mach number effects, Aerospace Science and Technology **8** (2004).

[31]B. Nishri and I. Wygnanski, Effects of periodic excitation on turbulent flow separation from a flap, AIAA Journal **36**, 547 (1998).

[32]J. Bernhardt and D. R. Williams, Closed-loop control of forebody flow asymmetry, AIAA Journal of Aircraft **37**, 491 (2000).

[33]W. E. Faller, S. J. Schreck, and M. W. Luttges, Neural network prediction and control of three-dimensional unsteady separated flowfields, Journal of Aircraft **32**, 1213 (1995).

[34]J. Ling and J. Templeton, Evaluation of machine learning algorithms for prediction of regions of high Reynolds averaged Navier Stokes uncertainty, Physics of Fluids **27**, 085103 (2015).

[35]B. Tracey, K. Duraisamy, and J. J. Alonso, A machine learning strategy to assist turbulence model development, AIAA Paper 2015–1287 (2015).

[36]T. G. Dietterich, Machine learning for sequential data: A review, in *Joint IAPR International Workshops on Statistical Techniques in Pattern Recognition (SPR) and Structural and Syntactic Pattern Recognition (SSPR)*, pp. 15–30, 2002.

[37]R. Semaan, P. Kumar, B. M. G. Tissot, L. Cordier, and B. R. Noack, Reduced-order modelling of the flow around a high-lift configuration with unsteady Coanda blowing, Journal of Fluid Mechanics **800**, 72 (2016).

[38]M. Burnazzi and R. Radespiel, Assessment of leading-edge devices for stall delay on an airfoil with active circulation control, CEAS Aeronautical Journal **5** (2014).